Magnetic properties and coupled spin-phonon behavior in quasi-one-dimensional screw-chain compound $BaMn_2V_2O_8$

Arkadeb Pal,[1,2,*] Khyati Anand,[2,*] T. W. Yen,[1] Atanu Patra,[3] A. Das,[4] S. M. Huang,[1] E. Blundo,[3] A. Polimeni,[3] H. D. Yang,[1,5,†] and Sandip Chatterjee[2,‡]

[1]*Department of Physics, National Sun Yat-sen University, Kaohsiung 804, Taiwan*
[2]*Department of Physics, Indian Institute of Technology (BHU), Varanasi 221005, India*
[3]*Physics Department, Sapienza University of Rome, 00185 Roma, Italy*
[4]*Solid State Physics Division, Bhabha Atomic Research Centre, Mumbai 400085, India and Homi Bhabha National Institute, Anushaktinagar, Mumbai 400094, India*
[5]*Center of Crystal Research, National Sun Yat-sen University, Kaohsiung 804, Taiwan*

(Received 6 August 2022; revised 24 November 2022; accepted 15 December 2022; published 10 January 2023)

Spin-chain compounds are known to exhibit fascinating magnetic properties, which mostly display magnetic ordering at very low temperatures or remain dynamic even at 0 K. In contrast, the present quasi-one-dimensional spin-chain system $BaMn_2V_2O_8$ exhibits a collinear antiferromagnetic (AFM) long-range ordering at a relatively higher temperature $T_N \sim 37$ K, wherein the nearest-neighbor spins have AFM coupling along the spin chain, i.e., along the c axis. The present study also reveals a short-range magnetic ordering prevailing at considerably elevated temperatures above its T_N. Temperature-dependent Raman spectroscopy demonstrates an occurrence of spin-phonon coupling below T_N at least for two phonon modes, whereas the study also shows an unusual thermal evolution of the Raman modes above T_N, which is apparently associated to the short-range magnetic ordering. Furthermore, extensive *ab initio* density functional theory calculations accompanied with classical Heisenberg model based theoretical calculations of various exchange interaction parameters (J_0–J_5) suggest an AFM ground state, which matches well with the experimentally obtained spin structure.

DOI: 10.1103/PhysRevMaterials.7.014402

I. INTRODUCTION

The study on low-dimensional magnetic systems has started seeking immense attention globally due to their intriguing rich magnetic phenomena [1–3]. They also hold promise for their potential applications in quantum computation [3]. The topology and dimensionality of such a spin system as well as its interactions occurring with other microscopic order parameters, such as lattice, charge, and orbital degrees of freedom, have a profound influence on its various aspects. In this regard, the research on the one-dimensional (1D) spin-chain systems has been a very active field of experimental as well as theoretical condensed matter physics. In a perfect 1D antiferromagnetic (AFM) spin system, the persistence of strong thermal and quantum fluctuations at low temperatures, which are triggered by macroscopic degeneracy, destroys the long-range ordering (LRO), leading to the well-known exotic phenomenon, spin liquid. Nevertheless, a real quasi-1D AFM spin system can exhibit a spin liquid state, or a three-dimensional (3D) Néel-type, or a XY-type magnetic ordering, which depend on various factors, such as the interchain interactions, magnetic anisotropy, and also spin values [4–6]. In fact, the half-integer spin-chain systems are gapless, wherein a finite interchain interaction leads to the LRO. On the contrary, an integer spin-chain system may exhibit a spin gap by showing a singlet ground state and triplet excited states.

In this context, a series of compounds having a chemical formula $AM_2V_2O_8$ (where A = Ba, Sr, Pb; and M = Co, Mn, Ni, Cu) attracted much interest owing to their distinct structures and varied intriguing magnetic properties. Their structure consists of arrays of edge-shared $M^{2+}O_6$ octahedra forming screw chains along the crystallographic c axis, leading to a quasi-1D structural arrangement of magnetic ions. Despite having similar crystal structures (although with different crystal symmetries), various $AM_2V_2O_8$ compounds display solely distinct magnetic properties, which vary with a change in the magnetic ions from Cu^{2+} to Mn^{2+}. The isolated spin dimer or alternating spin-chain system $BaCu_2V_2O_8$ shows a large spin gap with a singlet ground state [7]; the honeycomb magnetic system $BaNi_2V_2O_8$ shows a quasi-two-dimensional (2D) AFM ordering (XY type) [8], whereas the Haldane-gap spin-chain AFM systems $SrNi_2V_2O_8$ and $PbNi_2V_2O_8$ exhibit interesting quantum critical phase transition lying in between the spin liquid state and Ising-like magnetic state [9]. On the other hand, the Ising spin systems with strong magnetic anisotropy, viz., $BaCo_2V_2O_8$, $PbCo_2V_2O_8$, and $SrCo_2V_2O_8$ compounds display interesting field-driven quantum phase transition [10–12]. Interestingly, unlike the other members of the $AM_2V_2O_8$ family, the $S = 5/2$ spin-chain compounds, i.e., $SrMn_2V_2O_8$ ($T_N \sim 42.2$ K)

*These authors contributed equally to this work.
†yang@mail.nsysu.edu.tw
‡schatterji.app@iitbhu.ac.in

and $BaMn_2V_2O_8$ (BMVO) [$T_N \sim 37$ K] exhibit long-range AFM orders at much higher temperatures [13,14].

The compound BMVO was first synthesized in late 1992 by Von Postel and Müller-Buschbaum, who also deciphered its crystal structure [15]. However, its physical properties remained unexplored until He *et al.* reported its bulk magnetization and specific heat properties in late 2006 [14]. In their study, BMVO was shown to demonstrate a 3D long-range AFM ordering at $T_N \sim 37$ K. The observation of relatively high T_N was attributed to the enhanced interchain interactions owing to the larger spin moment of Mn^{2+} ions ($S = 5/2$). Nevertheless, a comprehensive study describing its microscopic spin structure and more detailed magnetic properties by using neutron diffraction measurements is still missing. This prompted us to investigate BMVO by employing neutron diffraction measurements. Moreover, it may also be interesting to estimate its various magnetic exchange interactions using theoretical calculations, which may be crucial for understanding its magnetic properties.

On the other hand, spin-phonon coupling (SPC) is a fascinating phenomenon of condensed matter physics that ensues from the renormalization of phonon modes by magnetic ordering. The SPC can also be a useful gauge for probing various intriguing phenomena, which include magnetostriction effect, spin Seebeck effect, thermal Hall effect, spin-Peierls transition, magnetoelectric effect, etc. [16,17]. The $AM_2V_2O_8$ compounds have been extensively studied mainly for their magnetic properties, whereas their other physical properties are not much explored. Regardless of the strong interactions between the lattice vibration and magnetism, the studies exploring the SPC remained largely undiscovered in the spin-chain materials. Meanwhile, the existence of the spin-lattice coupling and magnetoelectric effect has been recently reported in spin-chain compounds $NiTe_2O_5$ and Tb_2BaNiO_5 [18,19]. In this regard, the low-temperature Raman spectroscopy study of the BMVO system may be interesting, as its relatively high T_N renders it as a unique playground for studying the SPC phenomenon in this system. In this context, the present study provides insights into the physical properties of BMVO, especially detailed magnetic and lattice dynamics properties of this system, thus going beyond the existing knowledge of its bulk magnetization and specific heat results [14].

II. EXPERIMENTAL AND COMPUTATIONAL METHODS

A polycrystalline sample of BMVO was synthesized following a standard solid-state reaction method. High-purity oxide powders (>99.99%, Alfa Aesar) of $BaCO_3$, MnO, and V_2O_5 as starting materials were taken in a proper stoichiometric ratio, which was followed by a mixing and intimate grinding for 1 h. The mixture was pressed into pellets and thereafter they were subjected to several heating cycles with intermediate grindings at 750° C and 840° C for 48 h (at each cycle) under flowing Ar gas. The purity of the final product was verified by x-ray diffraction (XRD) using a D8 Advance Bruker diffractometer with Cu $K\alpha_1$ radiation. All the magnetization measurements were performed utilizing a superconducting quantum interference device (SQUID) based magnetometer (MPMS, Quantum Design). Temperature-dependent micro-Raman spectroscopy data were collected using a single-frequency Nd : YVO_4 laser (DPSS series by Lasos) having an excitation wavelength of 532.2 nm. For collecting all the Raman data, a laser beam of power 100 μW was focused onto a ∼2 μm diameter spot. The heating effect on target samples due to such a laser power was checked and found to be negligible. The data were recorded in backscattering geometry with the help of a monochromator (ACTON SP750), which is equipped with a 1200 groove mm^{-1} grating. The sample was cooled using a closed-cycle He cryostat (Montana Instruments, U.S.A.). Thermal contact of the sample with the cryostat platform was ensured by using a high-vacuum cryogenic heat grease, which maintained an optimal and fast heat exchange. To ensure the accuracy of the temperature, the sample was slowly cooled to each of the target temperatures, which was further followed by a 10 min waiting period prior to the collection of Raman data. The x-ray absorption spectra (XAS), which confirmed a nominal valence state of +2 for the Mn ions in BMVO, were collected in a total electron yield (TEY) mode at the BL20 beamline of the National Synchrotron Radiation Research Centre (NSRRC), Taiwan. The related discussions of XAS data have been provided in the Supplemental Material (SM) [20] (see also Refs. [21–25] therein). The neutron diffraction measurements were carried out by the PD2 neutron powder diffractometer ($\lambda = 1.2443$ Å) placed at the Dhruva reactor in the Bhabha Atomic Research Centre (BARC), Mumbai, India. The XRD and neutron powder diffraction (NPD) data were analyzed using the FULLPROF_SUITE program. It can be noted here that for all the Rietveld refinements of the NPD data, we did not refine the atomic position and B_{iso} parameters of atom "V," since its scattering length was too small for the neutron diffraction. Thus, we used the fixed values for the aforementioned parameters for atom V, which were obtained from the XRD data analysis at $T = 300$ K.

The *ab initio* DFT calculations were carried out utilizing the Vienna *ab initio* simulation package (VASP, version 6.1.2). More details of the calculations are provided in the SM [20].

III. RESULTS AND DISCUSSIONS

A. X-ray diffraction

Figure 1 depicts the XRD pattern of BMVO along with its Rietveld refinement at $T = 300$ K. The refinement of BMVO suggests a single-phase tetragonal structure with $I4_1cd$ symmetry (No. 110). No trace of any additional impurity peak is found, thus suggesting the pure phase formation of the sample. The obtained lattice parameters are $a = b = 12.612(1)$ Å and $c = 8.663(1)$ Å, which are in good agreement with the previous report [15]. The detailed crystal structure has been demonstrated in the following section.

B. Neutron diffraction: Crystal structure and microscopic spin structure

Furthermore, the neutron powder diffraction (NPD) measurements of BMVO have been performed at various temperatures (T) to understand the microscopic spin structure as well as the crystal structure. The Rietveld refinement of the NPD pattern collected at $T = 300$ K is shown in Fig. 2(a). All the

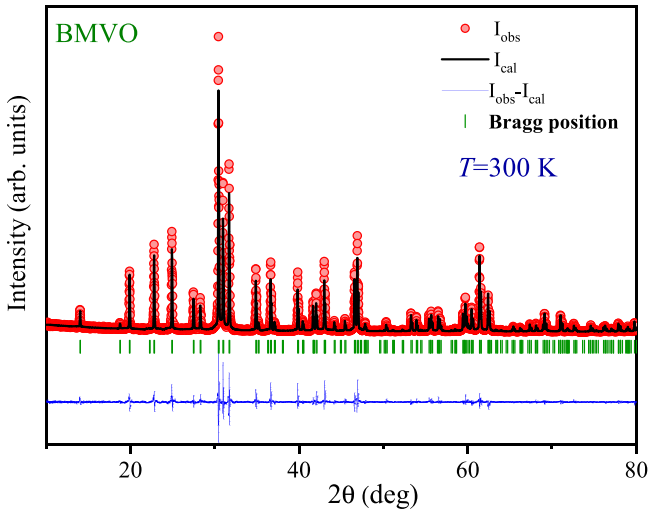

FIG. 1. Rietveld refinement of XRD pattern collected at room temperature (300 K) for BMVO. The red and black points represent the experimental XRD data and calculated profile, respectively. The green bars indicate the Bragg positions.

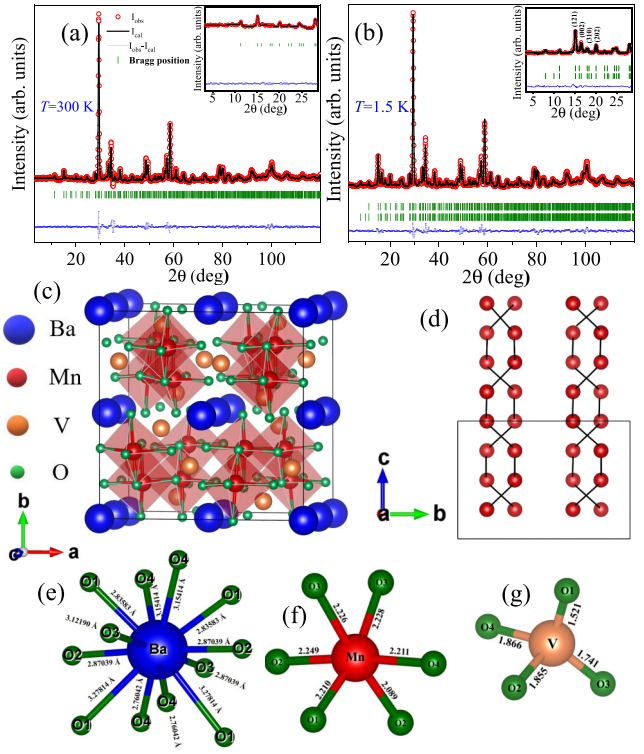

FIG. 2. (a,b) show the NPD data along with their Rietveld refinements at $T = 300$ and 1.5 K, respectively. The green bars show the Bragg positions. The insets of (a,b) show the close-up views of the aforementioned plots at lower angle ($2\theta < 27^\circ$), thus showing the appearance of magnetic reflections for the data at $T = 1.5$ K. (c) The pictorial representation of the unit cell. (d) shows a one-dimensional quasilinear chain that is formed by edge-sharing MnO_6 octahedra making a screw chain along the c axis expressed by the 4_1 screw symmetry axis. (e) Cuboctahedron of BaO_{12}; (f) MnO_6 octahedra; (g) VO_4 tetrahedron.

NPD data down to 40 K were fitted solely with the nuclear structure with symmetry $I4_1cd$. Figures 2(c)–2(g) demonstrate the crystal structure of BMVO as obtained from the NPD pattern (at 300 K) analysis. Figure 2(c) shows the unit cell, where the MnO_6 octahedra are shown in the ab plane. The basic polyhedral building blocks of the structure include a cuboctahedron of BaO_{12} [Fig. 2(e)], a sixfold oxygen coordinated MnO_6 octahedron [Fig. 2(f)], and a tetrahedron of VO_4 [Fig. 2(g)]. However, the aforementioned polyhedral blocks are slightly distorted, which is evident from the differences in various Ba−O, Mn−O, and V−O bond lengths [Figs. 2(e)–2(g)]. In this structure, a quasilinear-1D chain is formed by edge-sharing MnO_6 octahedra, thus leading to a screw chain along the c axis, which is expressed by the 4_1 screw symmetry axis [Fig. 2(d)]. There are four such spin chains (screw) in a unit cell that are centered at (0.25, 0.25, z), (0.25, 0.75, z), (0.75, 0.25, z), and (0.75, 0.75, z) on the ab plane. The Mn − Mn distance along a chain is found to be ~ 3 Å, whereas the distance between two chains (in the same ab plane) is around 6.6 Å. However, the minimum distance between two screw chains is ~ 5.16 Å, for which the two Mn ions are situated in two different ab planes separated by a distance of $c/4$. Therefore, the predominant magnetic interactions are expected to occur along the chain, whereas various weaker interchain superexchange interactions of similar strengths can take place among Mn spins via nonmagnetic VO_4 tetrahedra.

Furthermore, the emergence of a set of magnetic Bragg reflections [such as (002) and (310) near $2\theta \sim 16.5^\circ$ and 18°, respectively] as well as enhancements in some existing nuclear Bragg peaks [which include (121)/(211) near $2\theta \sim 15^\circ$ and (202)/(022) near $2\theta \sim 20^\circ$] are observed in the NPD patterns as temperature is cooled below 40 K, which is evident from Fig. 3(a). The aforementioned changes in the T dependence of the NPD patterns can be more clearly observed from the corresponding color-coded contour plot of the intensities of various NPD peaks as a function of T and 2θ, which is demonstrated in Fig. 3(b). This feature is typical of a LRO state of a magnetic system. This observation is consistent with the previously reported $T_N = 37$ K of BMVO, where its bulk magnetization and specific heat properties were investigated [14]. In their study, it was assumed that the LRO might have commenced at $T = 46$ K, which was fully developed below $T_N = 37$ K. This was based on the observation of a smeared anomaly in the specific heat study near 46 K and a sharp λ-like anomaly at 37 K. However, we could not detect any sizable magnetic signal of LRO in our NPD data collected at $T = 45$ K and it was only observed below $T = 40$ K, as evident from Figs. 3(a) and 3(b). Nevertheless, the present study confirms that the LRO state in BMVO is established below $T = 40$ K. The positions of the here observed magnetic Bragg peaks [for which the value of $h + k + l$ is an even integer] are also allowed by the body-centered (I) symmetry of the lattice. However, they are not allowed by the space group symmetry $I4_1cd$. Therefore, the NPD patterns recorded below $T = 40$ K could not be fitted with the nuclear structure alone; instead an additional contribution from magnetic ordering was also included by using a propagation vector $k = (0, 0, 0)$ with respect to the tetragonal symmetry. All the peaks were satisfactorily indexed with the aforementioned combination

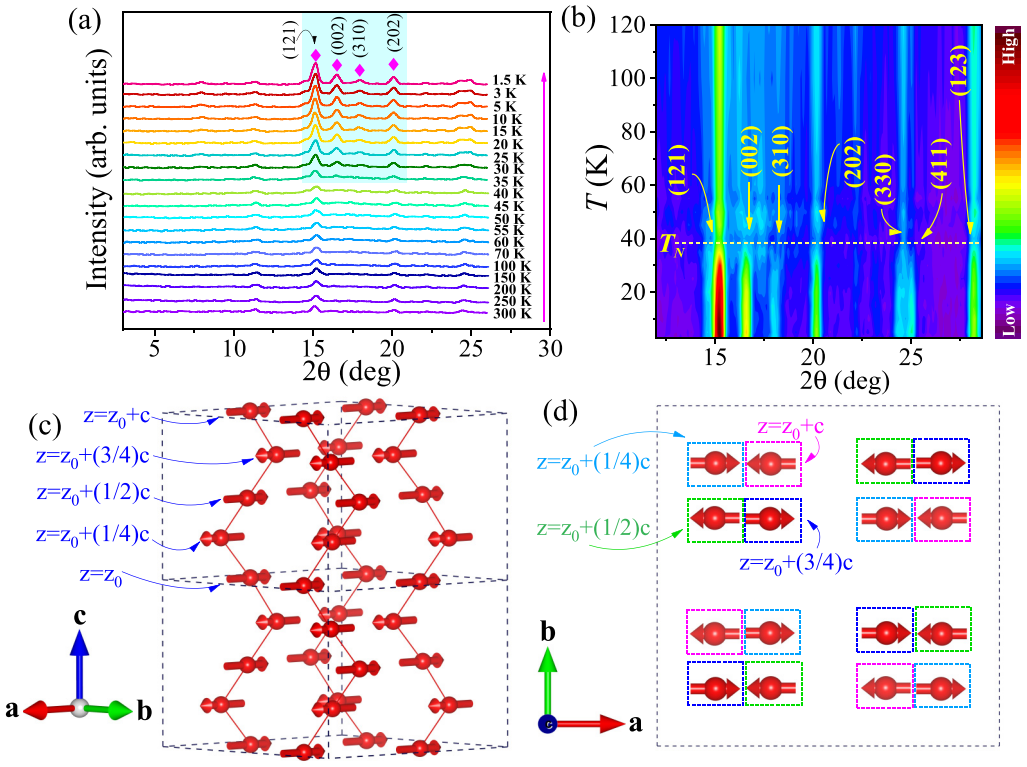

FIG. 3. (a) NPD patterns at different temperatures. The shaded region shows the onset of magnetic reflections below 40 K, thus suggesting the LRO below this temperature. (b) Color-coded contour plot of intensity of NPD peaks (related to magnetic ordering) as a function of temperature and angle (2θ). The plot clearly shows the appearance of magnetic Bragg reflections (002) and (310) as well as a rise in the intensities in some other peaks below $T_N \sim 37$ K. (c) demonstrates the microscopic spin structure of BMVO consisting of screw chains of Mn spins. The spins on each *ab* plane (i.e., at a fixed z) are parallel to each other, whereas the spins are antiparallel to each other along each individual screw chain, i.e., along the c axis. (d) depicts spin arrangements projected on the *ab* plane, i.e., as viewed along the c axis. In a unit cell, there are four screw chains, wherein the spins lying on the different *ab* planes, i.e., at $z = z_0 + (1/4)c$, $z = z_0 + (1/2)c$, $z = z_0 + (3/4)c$, and $z = z_0 + c$, are marked by dashed rectangles of blue (light), green, navy blue, and magenta, respectively.

fitting, which can be seen in Fig. 2(b) showing the NPD pattern at $T = 1.5$ K along with its Rietveld refinement. It is found that the positions of these magnetic peaks remain unaltered with lowering the temperature, thus confirming the k to be uniform down to $T = 1.5$ K. The unit-cell lattice constants, bond lengths, and bond angles, etc., as estimated from the NPD data analysis are summarized in Table I.

The spin structure as obtained from the NPD data (at $T = 1.5$ K) analysis has been schematically demonstrated in Figs. 3(c) and 3(d). The magnetic spins are parallel to each other on the *ab* plane; however, along the c axis (i.e., along the screw chain) the spins are antiparallel to each other. The best fit is obtained while a spin structure is considered, in which the spins are aligned perpendicular to the c axis—i.e., they are either along the a or b axis—while the moments along the other directions are considered to be zero or very weak. However, the precise determination of the moment direction along the a or b axis could not be done with the presented NPD patterns, as they were not in a feasible range. Nevertheless, it confirms that the spins are entirely on the *ab* plane.

Moreover, the thermal variation of the ordered magnetic moment (m) of Mn^{2+} ions, as determined from the NPD data analysis, rises below $T = 40$ K and it attains merely a saturation at lower temperatures, which can be seen from Fig. 4(a). The refined magnetic moment of the Mn^{2+} ions/site at $T = 1.5$ K is $\sim 2.4\,\mu_B/Mn^{2+}$, whereas the theoretically expected completely saturated moment of the Mn^{2+} ion is $5\,\mu_B (S = 5/2)$. The suppression in the moment value can be presumably attributed to the existence of strong quantum fluctuations owing to the quasi-1D nature of the present system, which hinders the spins attaining a fully ordered state. Generally, for a magnetic phase transition at $T = T_N$, the ordered moment follows the relation: $m \propto \sqrt{I}$, where I is the intensity of a magnetic reflection. For BMVO, the T variation of the normalized $\sqrt{I}$ of the (002) reflection (the normalization was done with respect to the peak at $T = 1.5$ K) displays a similar pattern [as shown in the inset of Fig. 4(a)] as that of m vs T, thus reasonably following the above relation. For the present case, the thermal variations of m and $\sqrt{I}$ below $T = 40$ K are qualitatively similar to that of other low-dimensional magnetic systems, including spin-chain compounds exhibiting second-order magnetic transitions [26–28]. The T-dependent specific heat studies of BMVO and its isostructural compound $SrMn_2V_2O_8$ were reported to display λ-like anomalies at their respective T_N, which also validated the second-order magnetic transitions in these systems [14,29]. Therefore, a second-order magnetic transition in BMVO can be inferred, which has been further analyzed using a critical exponent analysis in the following section.

TABLE I. Structural parameters of BMVO as determined from the Rietveld refinement of the NPD data at $T = 1.5$ and 300 K. Here, the atomic position of V shown in this table is not obtained from the NPD data analysis, whereas it is kept fixed at a position as determined from the XRD refinement at $T = 300$ K.

	Space group: $I4_1cd$	
Parameters	$T = 1.5$ K	$T = 300$ K
$a = b$ (Å)	12.5980(4)	12.6287(5)
c (Å)	8.6571(6)	8.6745(7)
Ba	8*a*	8*a*
X	0.0000	0.0000
Y	0.0000	0.0000
Z	0.0000	0.0000
B_{iso} (Å^2)	0.5000	0.5000
Mn	16*b*	16*b*
X	0.3352(13)	0.3284(17)
Y	0.3281(10)	0.3375(12)
Z	0.252(3)	0.255(4)
B_{iso} (Å^2)	0.51(13)	0.55(16)
V	16*b*	16*b*
X	0.25302	0.25302
Y	0.07669	0.07669
Z	0.11128	0.11128
B_{iso} (Å^2)	0.43110	0.43146
O(1)	16*b*	16*b*
X	0.1625(10)	0.1606(10)
Y	0.5070(9)	0.5050(9)
Z	0.0471(16)	0.0476(19)
B_{iso} (Å^2)	0.63(16)	0.39(12)
O(2)	16*b*	16*b*
X	0.3565(9)	0.3564(9)
Y	0.6708(12)	0.6708(12)
Z	0.5183(16)	0.516(2)
B_{iso} (Å^2)	1.3(2)	1.2(3)
O(3)	16*b*	16*b*
X	0.1653(8)	0.1669(8)
Y	0.6784(8)	0.6822(9)
Z	0.7572(15)	0.750(2)
B_{iso} (Å^2)	0.22(11)	0.14(15)
O(4)	16*b*	16*b*
x	0.3400(6)	0.3380(11)
y	0.4958(7)	0.4979(8)
z	0.2338(18)	0.236(2)
B_{iso} (Å^2)	–0.23(11)	0.77(14)
R_{wp}	6.60	6.67
GOF	1.72	2.00
χ^2	5.83	6.79

The order parameter (such as m) varies as a continuous function of T at a second-order magnetic phase transition, like the present case, whereas the critical properties are determined by a critical exponent β. The order parameter has a nonzero value in the magnetically long-range-ordered state, whereas it vanishes in the disordered or paramagnetic state. It is expressed as $m(T) = A(1-\frac{T}{T_N})^{\beta}$, where A is a proportionality constant. Figure 4(a) demonstrates the fitting of m vs T data using the aforementioned power law, which yielded $T_N = 36.7 \pm 0.8$ K and $\beta = 0.254 \pm 0.013$. The obtained value of T_N agrees well with the earlier reported transition temperature (37 K) of this system [14]. According to the dimensions of space and spins, magnetic systems are classified into several categories with different values of β, such as $\beta = 0.125$ (2D Ising), $\beta = 0.33$ (3D Ising), $\beta = 0.35$ (3D XY), $\beta = 0.36$ (3D Heisenberg), and $\beta = 0.5$ (mean field). Hence, for BMVO, the estimated value of $\beta = 0.254$ lies in an intermediate regime, i.e., in between the 2D and 3D Ising universality classes. Nevertheless, the observation of such a smaller value of β is not rare and similar unconventional values were previously reported in various other systems, including a recent work on a 1D spin-chain system, $NiTe_2O_5$ [19,27,30].

The raw neutron diffraction data at some selected temperatures are shown in Fig. 4(c). A broad humplike feature in the NPD pattern (as marked by the green dotted line for the data at $T = 35$, 40, and 70 K) is observed near $2\theta \sim 12^\circ - 25^\circ$ for a wide temperature range of 25−200 K. This is associated with a short-range magnetic ordering (SRO), which emerges due to the intrachain interactions at higher temperatures. At lower temperatures, the weaker interchain interactions may also contribute to the SRO. However, the system exhibits a 3D LRO state as the temperature is cooled below its T_N. The T variation of the intensity of the broad hump associated to the SRO has been shown in Fig. 4(b), which demonstrates the weakening of the diffused scattering below T_N, thus indicating the suppression of the SRO with the onset of the LRO AFM state. Nevertheless, the presence of the diffused scattering even below T_N can still be noted, which is also commonly observed in other low-dimensional and frustrated magnetic systems [13,28,31].

C. Magnetization

Figure 5(a) displays the T variation of dc magnetization (M) curves, i.e., $M(T)$ curves recorded under a magnetic field of $H = 2$ T, following the standard zero-field cooling (ZFC) and field cooling (FC) methods. The $M(T)$ curves show an increase in M with decreasing temperature, thereby attaining a plateau nearly below $T \sim 170$ K. This is typically observed in low-dimensional magnetic systems due to the emergence of SRO, which leads to the suppression of paramagnetic susceptibility. However, as the temperature is lowered further below $T \sim 120$ K, the magnetization starts increasing again, which is followed by an upturn near $T \sim 100$ K. We can reiterate that our NPD study revealed an enhanced SRO below $T \sim 100$ K [Fig. 4(b)]. Thus, a rise in the local short-range ferromagnetic (FM) ordering due to the enhanced interchain interactions may be a plausible reason for the exhibition of the increasing magnetization below $T \sim 100$ K. The observation of increasing magnetization due to SRO at temperatures above T_N was also previously reported in other systems [32–34]. Our Raman spectra analysis suggested a possible local structural distortion in the vicinity of $T \sim 100$ K (this will be discussed later), which may also be interlinked with the rise of SRO in this temperature region [35]. Moreover, a contribution from the orphan spins linked to some lattice defects may also have a role in showing the magnetization increase below 100 K. However, high-resolution synchrotron XRD and a single-crystal study may be required to unambiguously explain the above behavior. As the temperature is lowered

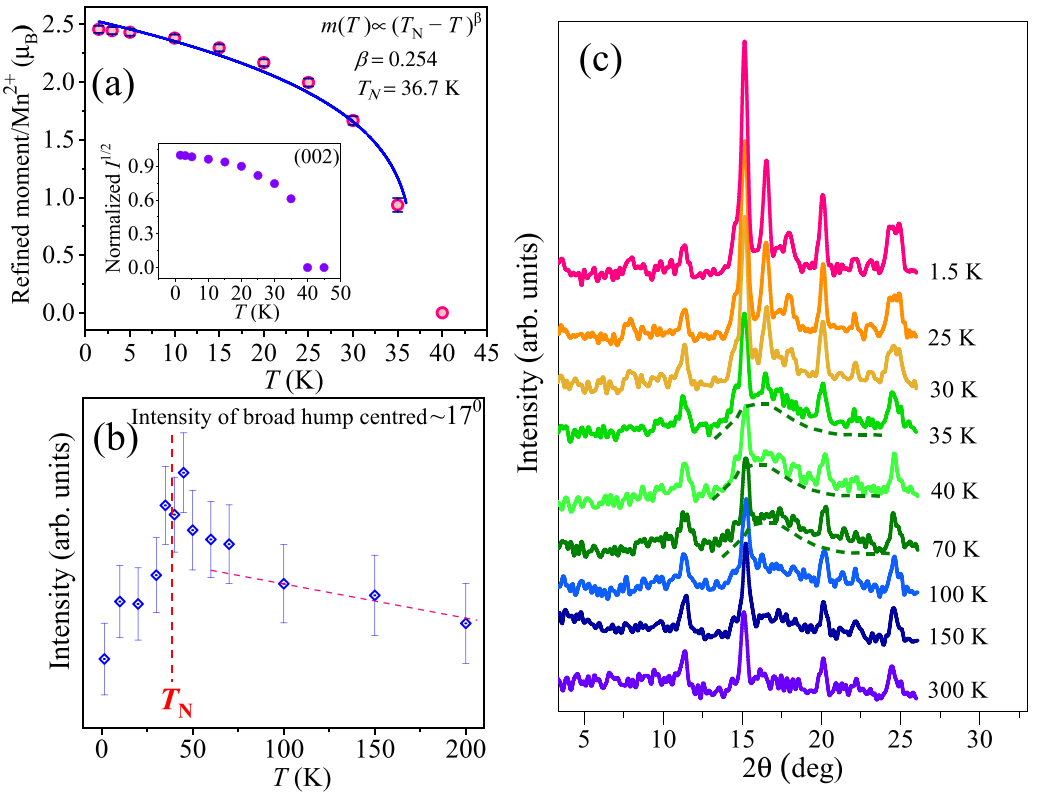

FIG. 4. Power-law fit (blue solid line) to the T variation of refined magnetic moment/Mn^{2+} data (red circles) to obtain the critical exponent. Inset: T dependence of normalized square root intensity, i.e., $\sqrt{I}$ of magnetic reflection (002). (b) The variation of the intensity of the humplike feature centered at $\sim 17^{\circ}$ (background) as a function of temperature. (c) The raw NPD data at some selected temperatures, wherein diffused scattering related to SRO (as indicated by the dotted green line) can be observed.

across $T_N \sim 37$ K, the $M(T)$ curve shows an anomaly in the form of a slight increase in magnetization, which essentially tracks the second-order magnetic transition in this system. The observed $T_N \sim 37$ K also agrees well with the earlier work [14]. At $T = 2$ K, under a high field of $H = 2$ T, the maximum value of magnetization observed is $\sim 0.1\,\mu_B$/f.u., which is only about 1% of the fully polarized magnetic moment expected for BMVO (i.e., $10\,\mu_B$/f.u.). Hence, this also suggests an AFM spin structure. The inverse susceptibility (χ^{-1}) vs T curve is shown in Fig. 5(b), which shows a clear deviation from linearity, thus violating the Curie-Weiss (CW) law (i.e., $\chi = \frac{C}{T-\theta_{CW}}$, where C denotes the Curie constant and θ_{CW} represents the CW temperature) even at elevated temperatures much higher than T_N. This can be attributed to the SRO prevailing above T_N. However, a CW fit was performed in a relatively narrow temperature range of $T = 240-300$ K, where the $\chi^{-1}(T)$ curve displayed linear behavior. The fitting yielded $\mu_{eff} = 6.306\,\mu_B$/Mn^{2+} and $\theta_{CW} = -464.08$ K. The theoretical spin-only moment of Mn^{2+} ions ($S = 5/2$) is $\mu_{theor} = 5.92\,\mu_B$/Mn^{2+}, which is slightly smaller than the experimentally obtained value of μ_{eff}. The existence of SRO above the T_N can essentially lead to such higher value of experimental μ_{eff} [27,36].

Figure 5(c) and its inset demonstrate the isothermal magnetic field (H) variation of magnetization curves, i.e., $M(H)$ curves at $T = 2$ and 300 K, respectively. At $T = 2$ K, the nonsaturating and merely linear nature of the $M(H)$ curve even at high fields further attests to the AFM nature of the system. The small hysteresis observed in the $M(H)$ curve may indicate the presence of a small spin canting. In fact, a canted AFM ordering of this system was also proposed in the earlier report showing similar $M(H)$ behavior [14]. The possible spin canting was attributed to the Dzyaloshinskii-Moriya (DM) interactions owing to the noncentrosymmetric nature of the crystal structure of BMVO. However, such a spin canting, if it exists, may be very small; thus the resulting signal was absent or minimal in the neutron diffraction data and it could not be detected in our NPD data analysis under the given resolution limit. The $M(H)$ curve recorded at 300 K shows typical paramagnetic behavior, which is expected at temperatures well above the T_N of this system.

D. Temperature-dependent Raman spectroscopy: Spin-phonon coupling

Figure 6 shows the room temperature (300 K) Raman spectrum of the BMVO system. The insets of Fig. 6 display the Lorentzian fits to the various observed Raman peaks in two different frequency ranges, $\omega \sim 300-500\,\text{cm}^{-1}$ (intermediate range) and $\omega \sim 750-920\,\text{cm}^{-1}$ (high-frequency range). The spectrum can be broadly divided into three bands centered near $\omega \sim 200$, 400, and $850\,\text{cm}^{-1}$, which are separated from each other by large gaps. The group theoretical symmetry analysis of the structure of BMVO having a space group $I4_1cd$ (No. 110) and a corresponding point group C_{4v} ($4mm$) predicts a total of 97 possible modes at its Γ

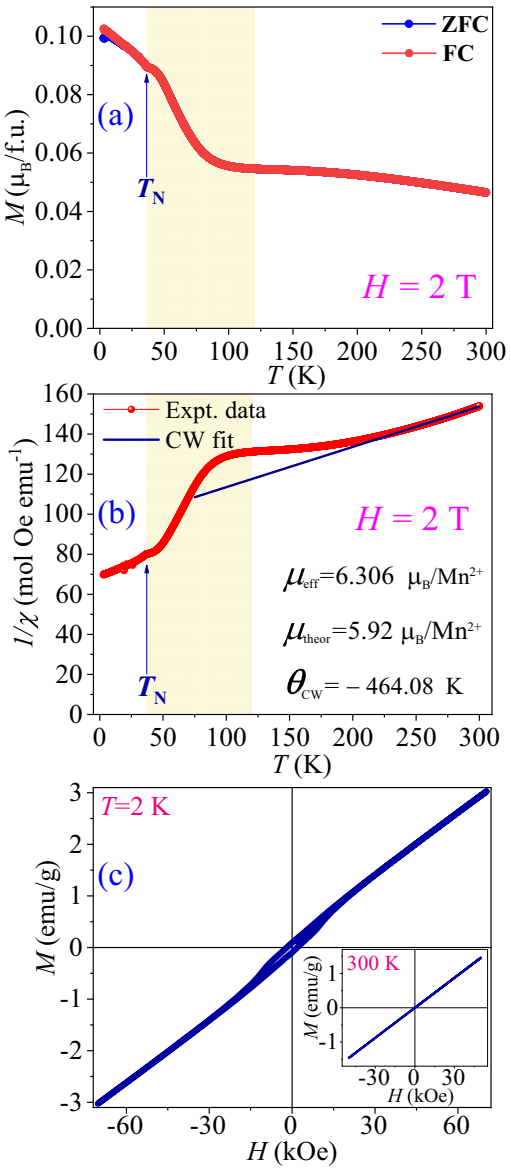

FIG. 5. (a) Thermal variation of magnetization (M) curves measured under $H = 2$ T following ZFC (blue) and FC (red) protocols. (b) Curie-Weiss fit (solid blue) to the inverse susceptibility ($1/\chi$) vs T curve (red) for the FC data. The shaded region in light yellow displays an enhanced SRO region. (c) Isothermal magnetization (M) curve with varying magnetic field (H) at $T = 2$ K. Inset: $M(H)$ curve collected at $T = 300$ K.

point of the Brillouin zone. These include 95 Raman active modes ($18A_1 + 19B_1 + 19B_2 + 39E$), of which 38 modes are exclusively Raman active ($19B_1 + 19B_2$), whereas 57 modes are simultaneously Raman and infrared (IR) active ($18A_1 + 39E$). In addition, there are two acoustic modes ($A_1 + E$). A qualitative discussion for phonon mode assignments to the observed Raman peaks is made in the SM [20].

Figure 7 shows temperature-dependent ($T = 6$–300 K) Raman spectra in three different frequency ranges, viz., low-frequency range ($\omega \sim 100$–$300\,\mathrm{cm}^{-1}$), midfrequency

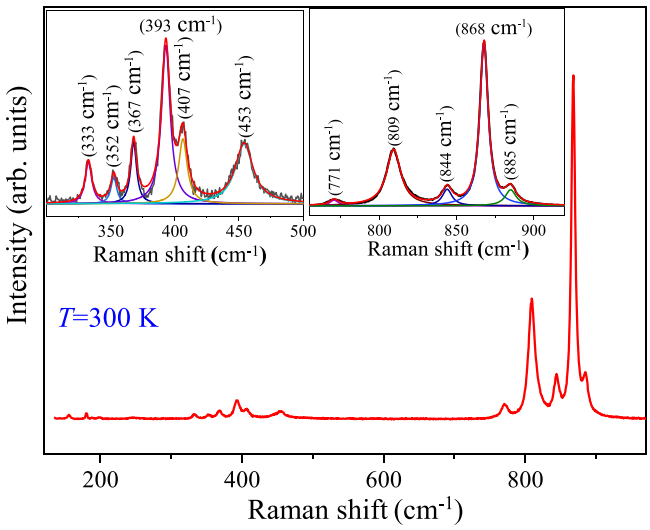

FIG. 6. Raman spectra at 300 K. Insets: Lorentzian fits of the observed peaks in the midfrequency range (left) and high-frequency range (right).

range ($\omega \sim 300$–$500\,\mathrm{cm}^{-1}$), and high-frequency range ($\omega \sim 720$–$920\,\mathrm{cm}^{-1}$). At the lowest temperature ($T = 6$ K), a total of 19 Raman modes are clearly observed, which have been denoted as P1–P19 (Fig. 7). All the Raman spectra show similar patterns throughout the temperature range of interest. However, during cooling, as the temperature crosses near $T \sim 125$ K, a peak splitting occurs near $\omega \sim 250\,\mathrm{cm}^{-1}$, thus leading to the formation of two new Raman modes, P5 and P6, as evident from Fig. 7. Moreover, another Raman mode (just above the P17 mode) lying around $\omega \sim 885\,\mathrm{cm}^{-1}$ at $T = 300$ K splits into two peaks, viz., P18 and P19, as the temperature cools to below nearly $T \sim 100$ K. A closer view of the aforementioned peak splitting is shown in Figs. 8(a) and 8(b). It can be reiterated that the magnetization as well as NPD data also indicated an enhancement of SRO roughly around $T \sim 100$ K. As there is no global structural change, the observation of the peak splitting (at temperatures near the enhanced SRO region) may be presumably attributed to a local structural distortion in the system, which can modulate the phonon spectra. This local structural distortion appears to emanate from the enhanced SRO in the system. In fact, the observation of peak splitting and/or the emergence of new Raman modes due to the local structural distortion, which is mediated by SPC related to SRO, was previously reported in other systems [37].

Furthermore, the thermal variations of the Raman shift (ω) and the corresponding full width at half maxima (FWHM) or linewidth (Γ) of various Raman modes (for $\omega > 300\,\mathrm{cm}^{-1}$) are shown in Figs. S3 and S4 of the SM, respectively [20]. A Lorentzian peak fitting was employed for the analysis. In general, for systems with magnetic atoms, $\omega(T)$ curves typically follow $\omega(T) = \omega_0 + \Delta\omega_{\mathrm{latt}}(T) + \Delta\omega_{\mathrm{anh}}(T) + \Delta\omega_{e-ph}(T) + \Delta\omega_{s-ph}(T)$, where ω_0 represents the frequency at an initial temperature T_0, $\Delta\omega_{\mathrm{latt}}$ is related to the lattice contraction or expansion, $\Delta\omega_{\mathrm{anh}}$ corresponds to the anharmonic contribution, and $\Delta\omega_{e-ph}$ and $\Delta\omega_{s-ph}$, respectively, denote the contributions

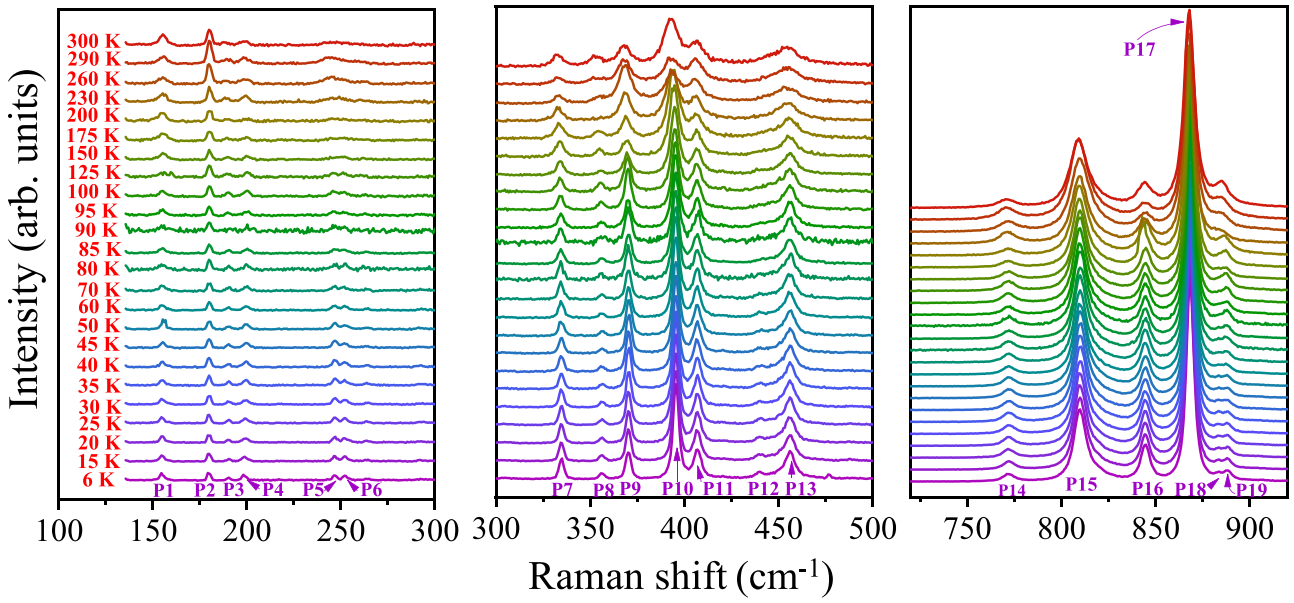

FIG. 7. Raman spectra at various temperatures in three different frequency ranges: 100–300, 300–500, and 720–920 cm^{-1}.

from the electron-phonon coupling and SPC [38]. Hence, in the absence of any structural change, SPC or electron-phonon coupling, or magnetostriction effect, $\omega(T)$ usually follows the anharmonic equation described as $\omega_{\mathrm{anh}}(T) = \omega_0 - C(1 + \frac{2}{e^{\frac{\hbar\omega_0}{2k_BT}}-1})$ [35,39–41], where C represents an adjustable fitting parameter, $\hbar$ denotes the reduced Planck's constant, and k_B represents the Boltzmann's constant. According to the anharmonic equation, the $\omega(T)$ curves should exhibit a hardening with decreasing T, thereafter attaining a lower-temperature plateau. For the present case, the Raman modes in the midfrequency range, i.e., P13, P11, P10, P9, and P7, show a clear hardening behavior, at least down to $T \sim 100$ K. For the Raman modes in the higher-frequency range; i.e., P17–P14, the $\omega(T)$ curves do not show a systematic thermal variation (except for the P14 mode), but display an overall increase at least down to T_N. Interestingly, for at least two modes, such as P9 and P15, a noticeable anomalous phonon softening is clearly visible in the vicinity of T_N, which are shown in Fig. 9. For the other modes, the observed anomalies are weak or minimal (Fig. S3 [20]). Moreover, an anharmonic fit to the $\omega(T)$ curve of the P9 mode shows a clear deviation below T_N [Fig. 9(a)]. Due to the highly insulating nature of the present system, the role of electron-phonon coupling can be ruled out for showing the anomalous phonon softening below T_N. In the absence of a structural change, the observed anomalous phonon softening below T_N may emanate from the SPC effect or magnetostriction. However, a magnetostriction effect is typically signaled by a remarkable anomaly in its unit-cell volume at T_N [40,42–44], which is not observed in the present system (Fig. S1 of the SM [20]). This clearly discards the magnetostriction effect in this system. Moreover, a magnetostriction effect does not affect the linewidths, i.e., $\Gamma(T)$ of the Raman modes, whereas a direct coupling between spin and phonon may lead to an anomaly in the $\Gamma(T)$ curves [37,42,44]. Nevertheless, the clear observation of the anomalous phonon softening at T_N for at least two Raman modes, i.e., P9 and P15, can be elucidated by a phonon modulation induced by the magnetic ordering, i.e., the SPC effect [38]. It is further noted that except for the P9 mode, for all the other modes, $\omega(T)$ curves do not clearly follow the anharmonic behavior even at high temperatures, which may also arise from the entangled spin and phonon parameters due to the presence of a strong SRO prevailing above T_N [37]. As the phonons get coupled to the spin degrees of freedom, the phonon renormalization occurs due to the modulation of spin correlation function $\langle S_iS_j\rangle$ (which refers to a statistical mechanical average for two adjacent spins, i.e., S_i and S_j) [45–47]. Thus, the phonon frequency shift ($\Delta\omega$) due to the SPC effect is given as follows: $\Delta\omega = -\lambda\langle S_iS_j\rangle = -\lambda S^2\varphi(T)$. Here, φ denotes

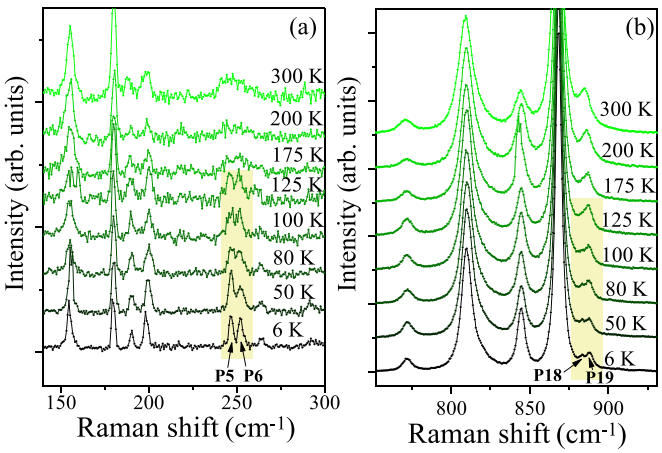

FIG. 8. Closer view of the Raman spectra at some selected temperatures near the peak splitting of P5–P6 and P18–P19. For the peaks P5–P6, the peaks split in the vicinity of $T = 125$ K, whereas for the P18–P19 peaks, the peak splitting commences around temperatures below $T = 100$ K.

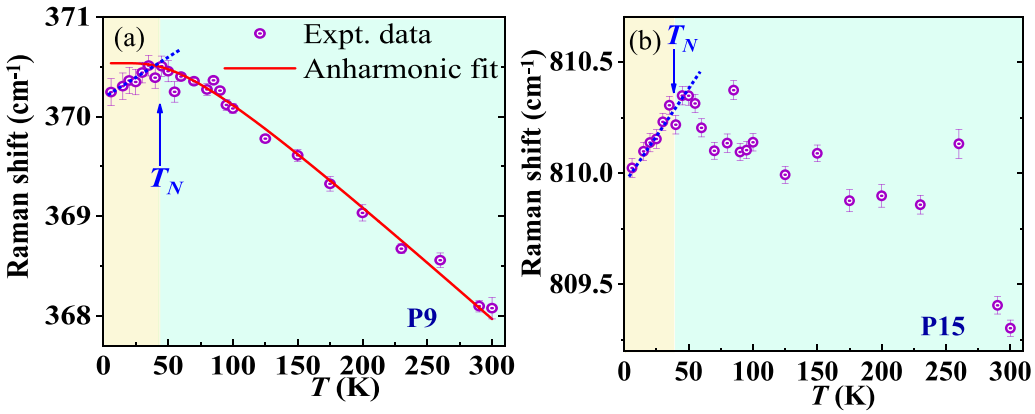

FIG. 9. Thermal variation of Raman shift for the (a) P9 and (b) P15 modes. For the P9 mode, a deviation from the anharmonic fit below T_N is demonstrated.

the short-range order parameter and λ represents the SPC constant. Using the mean field theory and the two-spin cluster method, Lockwood and Cottam determined the $\varphi(T)$ for two AFM systems, such as FeF_2 ($S = 2$) and MnF_2 ($S = 5/2$) [46]. This estimation of φ was subsequently used in other systems, as its value does not change significantly with changing S [37,48]. Thus, for the present case ($S = 5/2$), the reported value of φ can be reasonably used for the estimation of λ using the following relation: $\lambda = -\frac{\omega(T_{low})-\omega_{anh}(T_{low})}{[\varphi(T_{low})-\varphi(2T_N)]S^2}$. Here, $\omega(T_{low})$ denotes experimental phonon frequency at the lowest temperature measured (T_{low}), whereas $\omega_{anh}(T_{low})$ represents the corresponding value estimated from the anharmonic curve. The estimated value of SPC constant λ for the P9 mode is $\sim 0.06\,cm^{-1}$. This λ so obtained can be compared with some previously reported AFM compounds showing the SPC effect, such as MnF_2 ($\lambda = 0.4\,cm^{-1}$) [46], CuB_2O_4 ($\lambda = 0.02-0.03\,cm^{-1}$) [49], Ni_2InSbO_6 ($\lambda = 0.55-2.14\,cm^{-1}$) [39], Ni_2NbBO_6 ($\lambda = -0.3$ to $+0.67\,cm^{-1}$) [50], and 15R-$BaMnO_3$ ($\lambda = 1.2-3.8\,cm^{-1}$) [37], thus suggesting a weak SPC effect in BMVO.

As discussed in the SM [20], the Raman modes in the midfrequency range, including the P9 mode, involve MnO_6 vibrations. The modes in the high-frequency range, including the P15 mode, involve internal stretching vibrations of the $(VO_4)^{3-}$ units. As the long-range magnetic ordering sets in the system below T_N, the intrachain AFM exchange interactions among nearest-neighbor Mn spins occur via Mn−(O2)−Mn and Mn−O(3)−Mn exchange pathways, as demonstrated in Fig. S5(a) of the SM [20]. On the other hand, the interchain exchange interactions among Mn spins lying on different screw chains take place via various weaker exchange pathways, including Mn−O(4)−V−O(2)−Mn and Mn−O(1)−V−O(3)−Mn, which are created due to the presence of VO_4 tetrahedra joining these spins, as described in Fig. S5(b) of the SM [20]. Therefore, as the strong spin correlations ($\langle S_i S_j \rangle$) develop below T_N, it can essentially give rise to the phonon renormalization of the Raman modes involving MnO_6 and VO_4 vibrations [as all four O(1) to O(4) atoms participate in the magnetic exchange interactions] via the SPC effect, thus leading to the observed anomalous phonon softening below T_N.

However, detailed lattice dynamics calculations and T-dependent polarized Raman spectroscopy study may further help in getting a deeper insight into the mechanism of the SPC effect in BMVO. Nevertheless, the reports on the SPC effect in a spin-chain compound are very rare; thus the present observation of SPC in BMVO renders it among the rare materials. Our study unraveling the SPC in the present system may shed light on the understanding of such correlated behavior of different microscopic degrees of freedom in spin-chain systems.

E. Electronic density of states (DOS) and magnetic exchange interaction (J) calculations

We also carried out detailed density functional theory (DFT) based *ab initio* calculations of BMVO to gain a deep insight into its electronic and magnetic properties. The calculations are carried out both for the AFM (wherein the nearest-neighbor Mn spins are antiparallel to each other, thus leading to the experimentally obtained spin structure) and FM couplings among the Mn spins. Figures 10(a) and 10(b) demonstrate the total density of state (TDOS) along with the projected DOS (PDOS) for respective elements (Ba, Mn, V, and O) for the AFM and FM spin configurations, respectively, for the case of without spin-orbit-coupling (SOC) consideration. For both the AFM and FM cases, a large gap between the occupied and unoccupied electronic DOS is observed for both the up- and down-spin channels. This refers to the insulating nature of the system. The total energies of the system for both the AFM and FM cases are summarized in Table II, which shows that the AFM spin configuration with a lower energy is energetically favorable in this system, thus corroborating the experimental results.

Furthermore, the DOS results under the SOC considerations for the AFM and FM cases are shown in Figs. 10(c) and 10(d), respectively. For both the AFM and FM cases, the large gap in the DOS can be observed, which is increased slightly upon application of SOC. Our band-structure calculations also indicate the insulating nature of the system, which is shown in the SM [20]. The total energy for the AFM case still remains lower than that of the FM case, thus indicating an AFM ground state of the system. For all the above cases, a substantial hybridization between the Mn3d−O2p states and

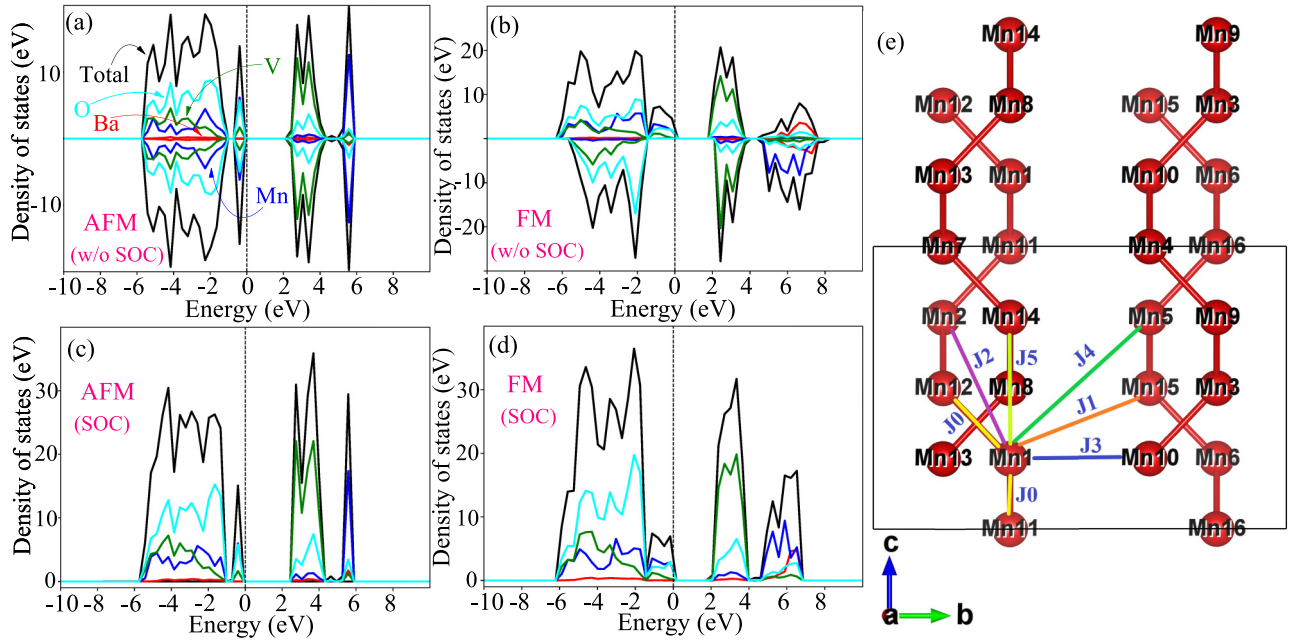

FIG. 10. Density of states (DOS) including TDOS and PDOS as obtained from the DFT calculations for (a) AFM and (b) FM spin configuration without considering the spin-orbit coupling (SOC). The calculated DOS for the AFM and FM spin configurations with SOC are shown in (c,d) respectively. The black line shows the total DOS (TDOS), whereas the projected DOS (PDOS) for different elements are shown in colored lines. (e) shows the four screw chains of Mn^{2+} ions in a unit cell, wherein various exchange interaction interactions (J_0–J_5) between various Mn^{2+} ions (viz., Mn1 − Mn16) are shown.

a finite hybridization between the V3d−O2p states are visible in the occupied DOS near E_F, thus providing exchange interaction pathways for the intrachain and interchain magnetic interactions.

As various competing intrachain and interchain exchange interactions (J) decide the magnetic ground state of a spin-chain compound, thus we further performed an extensive calculation to estimate these parameters. The details of the calculations are provided in the SM [20]. The exchange interactions (J_0–J_5) among different Mn ions, which have been estimated, are indicated in Fig. 10(e). The corresponding Mn−Mn pair distances are shown in Table III. The calculations suggest that the nearest-neighbor intrachain exchange interaction, i.e., $J_0 \sim +2.999$ meV, is the most dominant AFM interaction in BMVO, thus playing the pivotal role in determining its AFM ground state. Contradistinctively, the other magnetic exchange interactions (J_1–J_5) are much weaker as compared to J_0, which is evident from Table III. Thus, the results suggest that the spins in BMVO should stabilize in an AFM ordering, wherein the nearest-neighbor spins lie antiparallel to each other in a screw chain, thus agreeing with the NPD results. Therefore, in the present work, we demonstrate a comprehensive magnetic property study of BMVO by probing its nature of magnetic ordering and unfurling its microscopic spin structure through a combination of magnetization and neutron diffraction study, which is further supported by our theoretical exchange interaction energy calculations.

TABLE II. The total energy of BMVO for FM and AFM spin configurations under the consideration with and without SOC. Here, the AFM spin structure has antiparallel alignment of the nearest-neighbor spins along the spin chain.

Spin configuration	Total energy (eV)
FM without SOC	–765.95513
FM with SOC	–767.89258
AFM without SOC	–766.55335
AFM with SOC	–768.29068

IV. CONCLUSION

A quasi-one-dimensional noncentrosymmetric spin-chain compound $BaMn_2V_2O_8$ (BMVO) has been extensively studied by employing dc magnetization, neutron powder diffraction (NPD), x-ray absorption spectroscopy (XAS), and temperature-dependent Raman spectroscopy measurements, which were accompanied by comprehensive *ab initio* DFT calculations. Unlike most of the low-dimensional spin-chain compounds, BMVO exhibited a long-range AFM ordering at a

TABLE III. The exchange parameters index, distances among chosen pairs, and numerical values of J_0–J_5 from the numerical fitting are shown.

Exchange parameters index	Pair distance (Å)	J values (meV)
J_0	3.009	+2.99929
J_1	5.179	+0.04018
J_2	5.245	–0.57605
J_3	5.962	+0.10862
J_4	6.026	–0.03351
J_5	6.070	–0.03508

sufficiently higher transition temperature, i.e., $T_N = 37$ K. The NPD data analysis yielded a collinear AFM spin structure with the nearest-neighbor spins having an AFM coupling along the screw-chain axis of the system, whereas the spin direction lies along the *a* or *b* axis. The analysis further suggested that the AFM order in this spin-chain system developed with an unconventional critical exponent $\beta = 0.254$. A short-range magnetic ordering, much above the T_N, was also observed. The temperature-dependent Raman spectroscopy unraveled the exhibition of a pronounced spin-phonon coupling effect below T_N for at least two phonon modes. In addition, an unusual thermal evolution (such as violation of the anharmonic law and apparition of peak-splitting) of the Raman modes above T_N was observed, which might have a close correspondence with short-range magnetic ordering. Furthermore, the *ab initio* DFT calculations predicted an insulating AFM ground state of the system, which is in line with the experimental results. Moreover, our calculations showed that the nearest-neighbor intrachain exchange interactions (J_0) are the most dominating interactions to stabilize the observed AFM ground state in BMVO.

ACKNOWLEDGMENTS

S.C. acknowledges CIFC, IIT (BHU) Varanasi, for providing the magnetometer facility and he is also thankful to the FIST-DST, India, for providing funds for the research facilities in the Department of Physics, IIT (BHU) Varanasi. H.D.Y. and A. Pal acknowledge the support from Ministry of Science and Technology, Taiwan, under Grants No. MOST 111-2811-M-110 -012 and No. MOST 111-2112-M-110 -017. A. Polimeni, E.B., and A. Patra acknowledge support by Sapienza Università di Roma under the grant "Ricerche Ateneo" 2018.

[1] Y. Cui, H. Zou, N. Xi, Z. He, Y. X. Yang, L. Shu, G. H. Zhang, Z. Hu, T. Chen, R. Yu, J. Wu, and W. Yu, Quantum Criticality of the Ising-like Screw Chain Antiferromagnet $SrCo_2V_2O_8$ in a Transverse Magnetic Field, Phys. Rev. Lett. **123**, 067203 (2019).

[2] D. S. Inosov, Quantum magnetism in minerals, Adv. Phys. **67**, 149 (2018).

[3] V. Zapf, M. Jaime, and C. D. Batista, Bose-Einstein condensation in quantum magnets, Rev. Mod. Phys. **86**, 563 (2014).

[4] B. Pahari, K. Ghoshray, R. Sarkar, B. Bandyopadhyay, and A. Ghoshray, NMR study of ^{51}V in quasi-one-dimensional integer spin chain compound $SrNi_2V_2O_8$, Phys. Rev. B **73**, 012407 (2006).

[5] F. D. M. Haldane, Nonlinear Field Theory of Large-Spin Heisenberg Antiferromagnets: Semiclassically Quantized Solitons of the One-Dimensional Easy-Axis Néel State, Phys. Rev. Lett. **50**, 1153 (1983).

[6] F. D. M. Haldane, Continuum dynamics of the 1-D Heisenberg antiferromagnet: Identification with the O(3) nonlinear sigma model, Phys. Lett. A **93**, 464 (1983).

[7] Z. He, T. Kyômen, and M. Itoh, $BaCu_2V_2O_8$: Quasi-one-dimensional alternating chain compound with a large spin gap, Phys. Rev. B **69**, 220407(R) (2004).

[8] E. S. Klyushina, B. Lake, A. T. M. N. Islam, J. T. Park, A. Schneidewind, T. Guidi, E. A. Goremychkin, B. Klemke, and M. Månsson, Investigation of the spin-1 honeycomb antiferromagnet $BaNi_2V_2O_8$ with easy-plane anisotropy, Phys. Rev. B **96**, 214428 (2017).

[9] A. Zheludev, T. Masuda, I. Tsukada, Y. Uchiyama, K. Uchinokura, P. Böni, and S. H. Lee, Magnetic excitations in coupled Haldane spin chains near the quantum critical point, Phys. Rev. B **62**, 8921 (2000).

[10] Z. He, T. Taniyama, T. Kyômen, and M. Itoh, Field-induced order-disorder transition in the quasi-one-dimensional anisotropic antiferromagnet $BaCo_2V_2O_8$, Phys. Rev. B **72**, 172403 (2005).

[11] Z. He, T. Taniyama, and M. Itoh, Antiferromagnetic-paramagnetic transitions in longitudinal and transverse magnetic fields in a $SrCo_2V_2O_8$ crystal, Phys. Rev. B **73**, 212406 (2006).

[12] Z. He, Y. Ueda, and M. Itoh, Synthesis, structure and magnetic properties of new vanadate $PbCo_2V_2O_8$, J. Solid State Chem. **180**, 1770 (2007).

[13] A. K. Bera, B. Lake, W. D. Stein, and S. Zander, Magnetic correlations of the quasi-one-dimensional half-integer spin-chain antiferromagnets $SrM_2V_2O_8(M = Co, Mn)$, Phys. Rev. B **89**, 094402 (2014).

[14] Z. He, Y. Ueda, and M. Itoh, Magnetic properties of the quasi-one-dimensional system $BaMn_2V_2O_8$, Solid State Commun. **141**, 22 (2007).

[15] M. Von Postel and H. Müller-Buschbaum, Zur kenntnis von $Ba(MgZn)V_2O_8$, $BaMn_2V_2O_8$ und $Ba_{1/2}Sr_{1/2}Ni_2V_2O_8$, Z. Anorg. Allg. Chem. **615**, 97 (1992).

[16] S. F. Maehrlein, I. Radu, P. Maldonado, A. Paarmann, M. Gensch, A. M. Kalashnikova, R. V. Pisarev, M. Wolf, P. M. Oppeneer, J. Barker, and T. Kampfrath, Dissecting spin-phonon equilibration in ferrimagnetic insulators by ultrafast lattice excitation, Sci. Adv. **4**, eaar5164 (2018).

[17] X. Moya and N. D. Mathur, Turn your phonon, Nat. Mater. **16**, 784 (2017).

[18] R. Kumar, S. Rayaprol, S. Rajput, T. Maitra, D. T. Adroja, K. K. Iyer, S. K. Upadhyay, and E. V. Sampathkumaran, Existence of a critical canting angle of magnetic moments to induce multiferroicity in the Haldane spin-chain system Tb_2BaNiO_5, Phys. Rev. B **99**, 100406(R) (2019).

[19] A. Tiwari, D. C. Kakarla, G. Macam, C. H. Hsu, F. C. Chuang, H. C. Wu, T. W. Kuo, A. Pal, H. Chou, D. P. Gulo, H. L. Liu, Y. C. Chuang, Y. C. Lai, C. A. Lee, M. M. C. Chou, and H. D. Yang, Spin-lattice-charge coupling in quasi-one-dimensional spin-chain $NiTe_2O_5$, Phys. Rev. Mater. **6**, 044409 (2022).

[20] See Supplemental Material at http://link.aps.org/supplemental/10.1103/PhysRevMaterials.7.014402 for the additional details of the $V(T)$ curve, XAS, Raman mode assignment and their frequency and line width variations, and theoretical calculations methods.

[21] V. Kurnosov, V. Gnezdilov, P. Lemmens, Y. Pashkevich, A. K. Bera, A. T. M. N. Islam, and B. Lake, Phonon excitations in the quasi-one-dimensional Haldane phase of $SrNi_2V_2O_8$, Low Temp. Phys. **43**, 1405 (2017).

[22] A. Dubey and V. G. Sathe, The effect of magnetic order and thickness in the Raman spectra of oriented thin films of $LaMnO_3$, J. Phys.: Condens. Matter **19**, 346232 (2007).

[23] C. Roy and R. C. Budhani, Raman- and infrared-active phonons in hexagonal $BaMnO_3$, Phys. Rev. B **58**, 8174 (1998).

[24] R. B. Macedo Filho, A. Pedro Ayala, and C. William de Araujo Paschoal, Spin-phonon coupling in Y_2NiMnO_6 double perovskite probed by Raman spectroscopy, Appl. Phys. Lett. **102**, 192902 (2013).

[25] http://www.jass-code.org/index.php.

[26] A. M. Golubev, J. Nuss, R. K. Kremer, E. E. Gordon, M.-H. Whangbo, C. Ritter, L. Weber, and S. Wessel, Two-dimensional magnetism in α-CuV_2O_6, Phys. Rev. B **102**, 014436 (2020).

[27] J. H. Lee, M. Kratochvílová, H. Cao, Z. Yamani, J. S. Kim, J.-G. Park, G. R. Stewart, and Y. S. Oh, Unconventional critical behavior in the quasi-one-dimensional $S = 1$ chain $NiTe_2O_5$, Phys. Rev. B **100**, 144441 (2009).

[28] A. K. Bera, S. M. Yusuf, A. Kumar, M. Majumder, K. Ghoshray, and L. Keller, Long-range and short-range magnetic correlations, and microscopic origin of net magnetization in the spin-1 trimer chain compound $CaNi_3P_4O_{14}$, Phys. Rev. B **93**, 184409 (2016).

[29] S. K. Niesen, O. Heyer, T. Lorenz, and M. Valldor, Antiferromagnetic Heisenberg $S = 5/2$ spin chain compound $SrMn_2V_2O_8$, J. Magn. Magn. Mater. **323**, 2575 (2011).

[30] H. Takatsu, H. Yoshizawa, S. Yonezawa, and Y. Maeno, Critical behavior of the metallic triangular-lattice Heisenberg antiferromagnet $PdCrO_2$, Phys. Rev. B **79**, 104424 (2009).

[31] H. Yamauchi, D. P. Sari, I. Watanabe, Y. Yasui, L.-J. Chang, K. Kondo, T. U. Ito, M. Ishikado, M. Hagihara, M. D. Frontzek, S. Chi, J. A. Fernandez-Baca, J. S. Lord, A. Berlie, A. Kotani, S. Mori, and S. Shamoto, High-temperature short-range order in Mn_3RhSi, Commun. Mater. **1**, 43 (2020).

[32] Z. W. Ouyang, N. M. Xia, Y. Y. Wu, S. S. Sheng, J. Chen, Z. C. Xia, L. Li, and G. H. Rao, Short-range ferromagnetic correlations in the spin-chain compound Ca_3CoMnO_6, Phys. Rev. B **84**, 054435 (2011).

[33] K. Ghosh, C. Mazumdar, R. Ranganathan, and S. Mukherjee, Griffiths phase behaviour in a frustrated antiferromagnetic intermetallic compound, Sci. Rep. **5**, 15801 (2015).

[34] V. Hardy, V. Caignaert, O. Pérez, L. Hervé, N. Sakly, B. Raveau, M. M. Seikh, and F. Damay, Pretransitional short-range ordering in a triangular lattice of Ising spin chains, Phys. Rev. B **98**, 144414 (2018).

[35] A. Pal, T. W. Kuo, C.-H. Hsu, D. C. Kakarla, A. Tiwari, M. C. Chou, A. Patra, P. Yanda, E. Blundo, A. Polimeni, A. Sundaresan, F. C. Chuang, and H. D. Yang, Interplay of lattice, spin, and dipolar properties in $CoTeMoO_6$: Emergence of Griffiths-like phase, metamagnetic transition, and magnetodielectric effect, Phys. Rev. B **105**, 024420 (2022).

[36] A. K. Pramanik and A. Banerjee, Finite-size effect on evolution of Griffiths phase in manganite nanoparticles, J. Phys.: Condens. Matter **28**, 35LT02 (2016).

[37] B. Poojitha, A. Rathore, A. Kumar, and S. Saha, Signatures of magnetostriction and spin-phonon coupling in magnetoelectric hexagonal 15-$R$$BaMnO_3$, Phys. Rev. B **102**, 134436 (2020).

[38] E. Granado, A. García, J. A. Sanjurjo, C. Rettori, I. Torriani, F. Prado, R. D. Sánchez, A. Caneiro, and S. B. Oseroff, Magnetic ordering effects in the Raman spectra of $La_{1-x}Mn_{1-x}O_3$, Phys. Rev. B **60**, 11879 (1999).

[39] M. A. Prosnikov, A. N. Smirnov, V. Y. Davydov, Y. Araki, T. Arima, and R. V. Pisarev, Lattice and magnetic dynamics in the polar, chiral, and incommensurate antiferromagnet Ni_2InSbO_6, Phys. Rev. B **100**, 144417 (2019).

[40] A. Pal, C. H. Huang, T. W. Yen, P. H. Lee, Y. H. Chang, C. H. Yeh, T. W. Kuo, A. Tiwari, D. C. Kakarla, S. M. Huang, M. C. Chou, H. S. Kunwar, S. Rana, V. G. Sathe, B. H. Chen, Y. C. Chuang, and H. D. Yang, Spin-induced strongly correlated magnetodielectricity, magnetostriction effect, and spin-phonon coupling in helical magnet $Fe_3(PO_4)O_3$, Phys. Rev. B **106**, 094404 (2022).

[41] K. Anand, A. Pal, M. Alam, S. Dan, S. Kumar, S. Ghosh, S. Kumari, A. Das, M. Sawada, A. Mohan, V. G. Sathe, and S. Chatterjee, Emergence of metamagnetic transition, re-entrant cluster glass and spin phonon coupling in Tb_2CoMnO_6, J. Phys.: Condens. Matter **33**, 275802 (2021).

[42] A. Nonato, B. S. Araujo, A. P. Ayala, A. P. Maciel, S. Yanez-Vilar, M. Sanchez-Andujar, M. A. Senaris-Rodriguez, and C. W. A. Paschoal, Spin-phonon and magnetostriction phenomena in $CaMn_7O_{12}$ helimagnet probed by Raman spectroscopy, Appl. Phys. Lett. **105**, 222902 (2014).

[43] V. Srinu Bhadram, B. Rajeswaran, A. Sundaresan, and C. Narayana, Spin-phonon coupling in multiferroic $RCrO_3$ (R-Y, Lu, Gd, Eu, Sm): A Raman study, Europhys. Lett. **101**, 17008 (2013).

[44] A. Pal, S. Ghosh, A. G. Joshi, S. Kumar, S. Patil, P. K. Gupta, P. Singh, V. K. Gangwar, P. Prakash, R. K. Singh, E. F. Schwier, M. Sawada, K. Shimada, A. K. Ghosh, A. Das, and S. Chatterjee, Investigation of multi-mode spin–phonon coupling and local B-site disorder in Pr_2CoFeO_6 by Raman spectroscopy and correlation with its electronic structure by XPS and XAS studies, J. Phys.: Condens. Matter **31**, 275802 (2019).

[45] A. B. Sushkov, O. Tchernyshyov, W. Ratcliff II, S. W. Cheong, and H. D. Drew, Probing Spin Correlations with Phonons in the Strongly Frustrated Magnet $ZnCr_2O_4$, Phys. Rev. Lett. **94**, 137202 (2005).

[46] D. J. Lockwood and M. G. Cottam, The spin-phonon interaction in FeF_2 and MnF_2 studied by Raman spectroscopy, J. Appl. Phys. **64**, 5876 (1988).

[47] J. S. Lee, T. W. Noh, J. S. Bae, I.-S. Yang, T. Takeda, and R. Kanno, Strong spin-phonon coupling in the geometrically frustrated pyrochlore $Y_2Ru_2O_7$, Phys. Rev. B **69**, 214428 (2004).

[48] D. J. Lockwood, Spin–phonon interaction and mode softening in NiF_2, Low Temp. Phys. **28**, 505 (2002).

[49] R. D. Mero, C.-H. Lai, C.-H. Du, and H.-L. Liu, Spectroscopic Signature of SpinChargeLattice Coupling in CuB_2O_4, J. Phys. Chem. C **125**, 4322 (2021).

[50] M. A. Prosnikov, A. N. Smirnov, V. Yu. Davydov, R. V. Pisarev, N. A. Lyubochko, and S. N. Barilo, Magnetic dynamics and spin-phonon coupling in the antiferromagnet Ni_2NbBO_6, Phys. Rev. B **98**, 104404 (2018).